

Defect Detection and Identification of Point-Focusing Shear-Horizontal EMAT for Plate Inspection

Songling Huang, *Senior Member, IEEE*, Hongyu Sun, Lisha Peng, Shen Wang,
Qing Wang, *Senior Member, IEEE*, and Wei Zhao

Abstract—As a kind of nondestructive testing (NDT) method, shear-horizontal (SH)-guided wave detection technology is widely used on an electromagnetic acoustic transducer (EMAT). Although ultrasonic-guided waves perform well in defect location, it is difficult to obtain detailed information about defects, and the low efficiency of EMAT energy conversion still reduces the EMAT's performance. Therefore, in this work, the defect detection method of different shapes and sizes by point-focusing shear-horizontal (PFSH)-guided wave EMAT with the use of periodic permanent magnet (PPM) is investigated through simulation and experiment. For the purpose of defect classification and quantification, the extraction principles of defect features are obtained through simulation based on the circumferential scatter diagrams, and the neural network (NN) is used to process the features extracted from the experimental data. The results show that by extracting effective defect features from the scatter diagram, high-accuracy classification and high-precision quantification of defects under the influence of the focusing transducer can be achieved.

Index Terms—Acoustic sensors, acoustic waves, focusing, feature extraction, machine learning (ML), sensor phenomena and characterization.

I. INTRODUCTION

IN INDUSTRIAL production, since aluminium has good electrical conductivity, corrosion resistance, and low density, it has been applied in a host of fields such as construction and electronic communication. However, in the processing and use of aluminum plates, defects such as cracks, corrosion, and perforations in the plates inevitably appear, which affect the safe use of the plates. Accordingly, it is indispensable to use effective nondestructive testing (NDT) techniques to detect defects of the specimen efficiently [1]–[5]. Commonly used NDT methods include magnetic flux leakage (MFL) [6], X-ray, eddy current [7], [8], and ultrasonic testing. MFL detection is arduous to perform in the high-velocity detection due to its detection accuracy and speed limitation, and it is impossible to

This work was supported by the National Natural Science Foundation of China (NSFC) under Grant 52077110 and Grant 52007088.

Songling Huang, Hongyu Sun, Lisha Peng, Shen Wang, and Wei Zhao are with the State Key Laboratory of Power System, Department of Electrical Engineering, Tsinghua University, Beijing 100084, China (e-mail: huangsling@mail.tsinghua.edu.cn).

Q. Wang is with the Department of Engineering, Durham University, Durham DH1 3LE, U.K.

Detect nonferromagnetic specimens, Radiation detection has a long period and is detrimental to the health of the human body. The ultrasonic detection has high sensitivity, high speed, deep penetration, and is suitable for detecting both internal and external surface defects, so it has significant advantages in aluminum plate flaw detection.

As an ultrasonic NDT method, ultrasonic-guided wave detection has the advantages of long propagation distance, low attenuation, high speed, and high efficiency [9]. At present, methods commonly used to generate ultrasonic-guided waves include the piezoelectric ultrasonic method and electromagnetic ultrasonic method. Although the piezoelectric transducer has a higher signal intensity and detection sensitivity, the presence of the couplant makes it challenging to apply in the detection of complex high-temperature environments [10]. Moreover, as one of the widely used guided waves, due to the principal limitation, the shear horizontal (SH)-guided wave is difficult to be generated by the piezoelectric transducer [11]. Compared with piezoelectric transducers, electromagnetic acoustic transducers (EMATs) exhibit the following advantages: do not need a couplant, mode controllable [5], and no surface treatment required. However, this noncontact detection method has a low energy conversion efficiency, and it is difficult to determine the shape and size of the defects.

As a mode that an EMAT could easily generate, the SH-guided wave has the features of simple dispersion characteristics, no off-plane displacement, and does not generate mode conversion, so it is widely used in the defect detection [12]. Vasile proposed the periodic permanent magnet (PPM) EMAT with the use of the Lorentz force mechanism to excite SH₀ mode-guided waves [13]. However, this study did not mention the performance of the PPM EMAT in actual testing. In pipeline inspection, Hirao and Ogi used SH-guided waves to detect defects on the outer surface of the steel pipe with the use of a PPM EMAT, which could excite and receive SH-guided waves along the circumference direction [14]. However, the problem of low EMAT energy conversion efficiency remains unresolved. Specifically, in previous studies, we proposed a point-focusing SH (PFSH) EMAT to improve the transducer's focusing performance by using a PPM EMAT [15]–[17]. Although the detection of defects by SH-guided waves has been extensively studied, the response of the new PFSH-EMAT to defects has not been reported to our knowledge [18]–[22].

In addition, the further judgment of defects, such as classification and quantification, requires a lot of manual decision-making, which is time-consuming and related to the operator's subjective experience. Therefore, a variety of automated decision support methods based on feature

extraction and machine learning (ML) have been proposed [23], [24]. However, the feature extraction method of the signal received by the PFSH-EMAT is rarely studied, because the characteristics of the defect echo received by the special transducer are difficult to extract from the signal received by a single transducer. Therefore, combining the circumferential scatter diagram-based defect discriminating features, by reasonably selecting the characteristics of the experimental signals and using neural network (NN) algorithms, the defect classification and quantification can be realized.

Therefore, in this work, a PFSH-EMAT with the use of PPM is used to detect defects of different sizes and shapes on the aluminum plate, and the preliminary research has been published in our conference abstract [25]. The reflected signals from the cuboid and cylinder penetration defects are obtained from the finite-element method (FEM) and experiment. The effect of different defect sizes on the amplitude of the reflected wave amplitude is investigated. By reasonably selecting the receiving circle, the circumferential scatter pattern of the defect reflection signal is drawn, thereby further distinguishing the shape and size of the defect. After that, to further verify the proposed defect identification method, NN is used to train the features extracted from the experimental data. In addition, the weights of NN neurons are extracted to verify the proposed defect classification and quantification method.

II. DESIGN OF PFSH-EMAT

Before investigating the detection of defects by PFSH-EMAT, it is necessary to demonstrate the structure of the transducer. Fig. 1(a)–(c) manifest the front view, top view, and 3-D model of a PFSH-EMAT. The fan-shaped PPM is used to provide the bias magnetic field. The lengths of the individual coils are the same, thereby ensuring that the phase of the guided waves reaching the focal point is uniform. Burst current is applied on the coil to induce the eddy current on the specimen. Accordingly, the eddy current generates pulsed Lorentz forces under the bias magnetic field of the PPM, thereby exciting the SH-guided wave in the aluminium plate.

In order to focus the generated SH-guided waves into a specific area, the concentric coils are arranged, and the focal position is the center of the fan-shaped PPM. The magnet spacing is half the shear wave wavelength to enable phase consistency. Here the propagation direction of the SH wave is defined as the x -axis, the polarization direction is the y -axis, and the surface normal direction is the z -axis. The aperture angle is defined as the angle of the concentric coils, and the focal length is the distance from the focal point to the middle of the PPM.

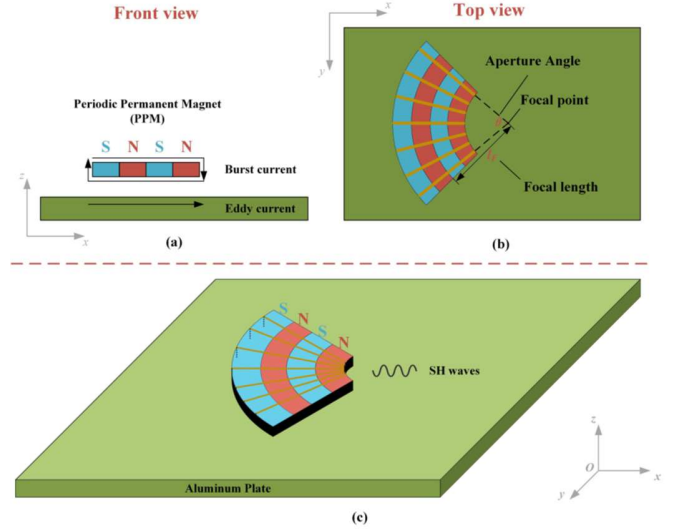


Fig. 1. Configuration of the PFSH-EMAT. (a) Front view. (b) Top view. (c) 3-D model.

In order to obtain the characteristics of the SH-guided wave when it encounters defects, all parameters of the transducer are fixed: excitation current amplitude $I = 50$ A, current frequency $f = 1$ MHz, aperture angle $\theta = 60^\circ$, focal length $l_f = 100$ mm, coil turns number $n = 7$, lift-off distance $d = 1$ mm, and remanence magnetism of the PPM $B = 1.2$ T. To study the general rules of defect detection, these parameters are set to values within a feasible interval to ensure the recognizability of the received signal. To further obtain the optimal value, the orthogonal test method can be considered to obtain the optimal combination of parameters [26].

III. ANALYSIS OF REFLECTED SIGNAL

A. Simulation Method

An EMAT uses the electromagnetic coupling to enable energy transfer, rather than a couplant. The material of the metal plate used in this study is aluminium, which is not ferromagnetic. Specifically, this physical process could only be described by the Lorentz force theory, and the magnetization and magnetostriction mechanisms are not considered. When the pulsed current passes through the coils, a corresponding eddy current \mathbf{J}_e is induced inside the aluminium plate [27]

$$\mathbf{J}_e = -\sigma \frac{\partial \mathbf{A}}{\partial t} \quad (1)$$

where \mathbf{A} indicates the magnetic field potential, σ is the conductivity, and t is the time. Due to the presence of the bias magnetic field provided by the PPM, eddy current \mathbf{J}_e will interact with it to generate the Lorentz force \mathbf{F}_L

$$\mathbf{F}_L = \mathbf{J}_e \times (\mathbf{B}_d + \mathbf{B}_s) \quad (2)$$

where \mathbf{B}_s represents the static magnetic field and \mathbf{B}_d is the dynamic magnetic field. Accordingly, the pulsed Lorentz force generated by the pulsed eddy current under the bias magnetic field generates the vibration displacement \mathbf{u} in the aluminium

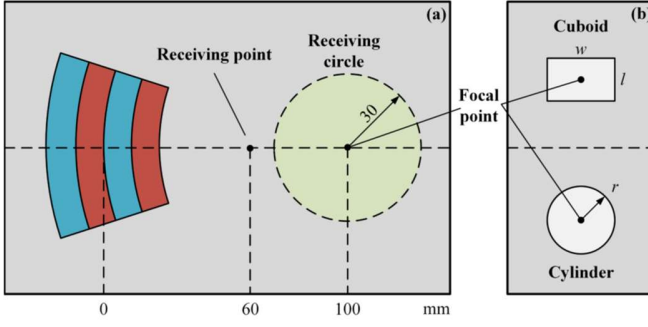


Fig.2. Configuration of the simulation process. (a) Receiver arrangement of guided wave signals. (b) Definition of defect shape, size, and position..

plate, thereby exciting the ultrasonic waves. The following wave equation could describe this process.

$$(\kappa + G)\nabla\nabla \cdot \mathbf{u} + G\nabla^2\mathbf{u} + \mathbf{F}_L = \rho \frac{\partial^2\mathbf{u}}{\partial t^2} \quad (3)$$

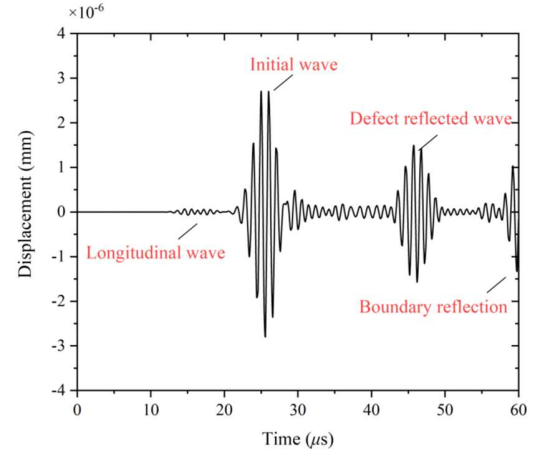
where \mathbf{u} is the displacement vector, t is the time, ρ is the mass density, and κ and G are the Lamé's constants of the material, which affects the propagation velocity of the shear and longitudinal waves in the specimen.

It can be seen that (2) connects two equations, including (1) that is described by the Maxwell equations and (3) that is described by the wave equation. To solve these partial differential equations, the FEM is selected as an effective tool by using COMSOL software. COMSOL is widely used in scientific research, and multiphysical coupled governing equations describing the physical process of the EMAT could be fully solved in this software. It is worth noting that the receiving process of an EMAT is the inverse of the transmitting process [21], [28], [29].

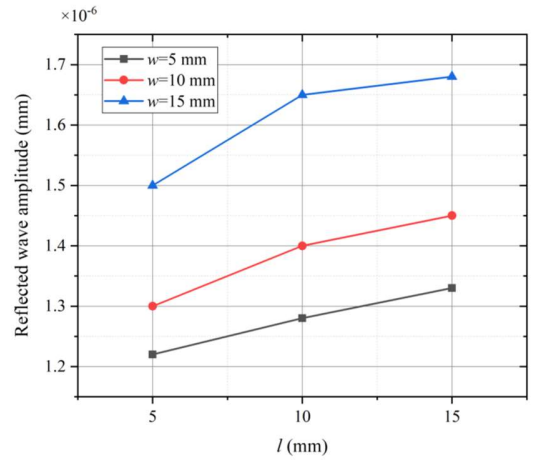
Fig. 2 shows the configuration of the simulation process. In Fig. 2(a), the center of the PPM is set to the coordinate origin, the focal position is 100 mm from the origin, and the receiving point is located 40 mm from the focal point. The receiving circle with a radius of 30 mm is used to measure the refraction, scattering, and transmission processes of ultrasonic-guided waves in different directions. Fig. 2(b) shows the defect on the plate, and it should be noted that the types of defects studied in this article are all through-hole defects. The center of the defect is consistent with the focal point, and the cuboid defect has a width of w and length of l , and the cylinder defect has a radius of r . The depths of all the defects are the same as the plate thickness (1.5 mm).

B. Helical Routes Separation

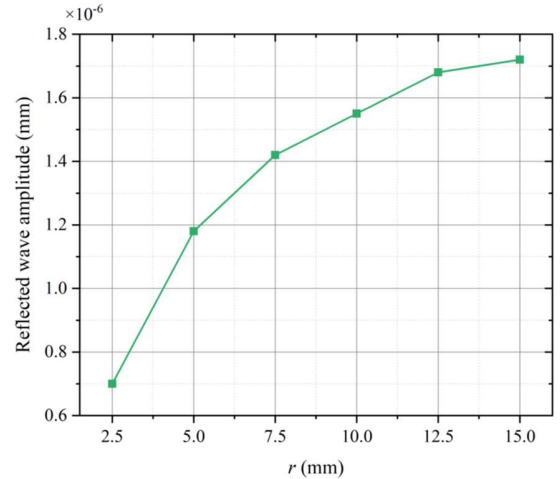
The cylinder defect with a radius of 10 mm is selected as a particular case to calculate the numerical model. Using the methods above, the displacement at the receiving point is shown in Fig. 3(a). It could be seen from the figure that the longitudinal wave reaches the receiving point before the shear wave because the wave velocity of the longitudinal wave in the aluminum plate is about twice that of the shear wave. The initial waves reach the receiving point at around 25 μs , and the reflected



(a)



(b)



(c)

Fig.3. Simulation results of the PFSH-EMAT. (a) Displacement at the receiving point, where the longitudinal, initial, defect reflected, and boundary reflection waves are presented. (b) Results of cuboid defects with different sizes. (c) Results of cylinder defects with different radii..

waves from the defect are at about 45 μs . Considering the defect radius, after the shear waves reach the receiving point, the distance to the defect edge and then back to the receiving point is 60mm. It could be calculated that the time difference is about 20 μs , thus demonstrating the rationality of the simulation

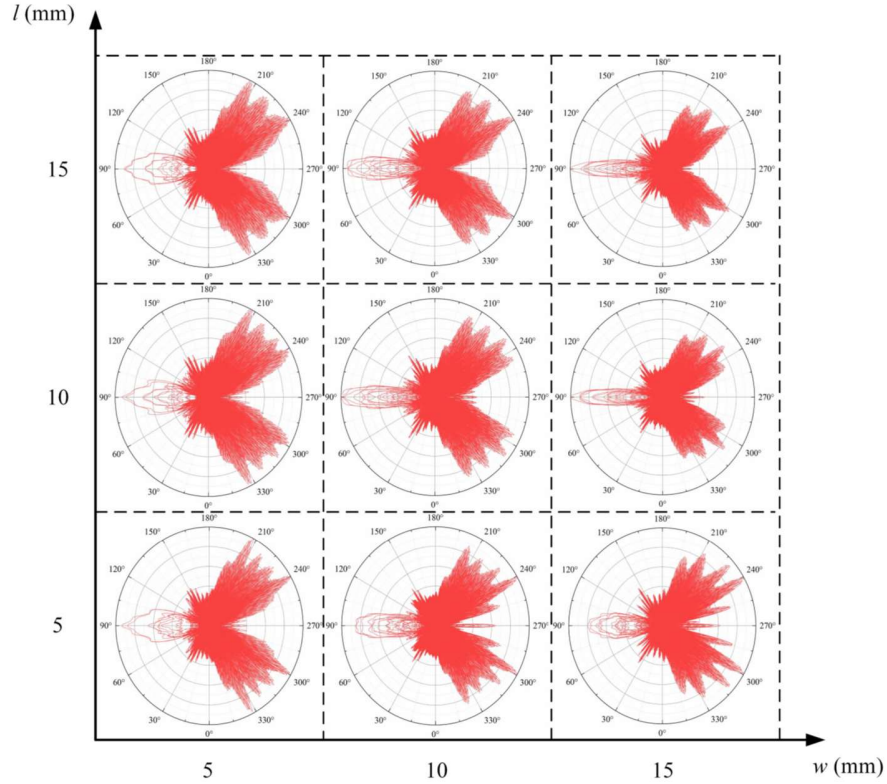


Fig.4. Circumferential scatter diagrams of the cuboid defects with different sizes..

Results. Although the actual aluminum plate is much larger, due to the size limitation, there are reflected waves from the boundary of the aluminum plate, as shown in Fig. 3(a). Since the boundary reflection waves do not affect the result, and the initial wave amplitude is also independent of the defect, so only the defect reflection waves are considered in the study.

To obtain the reflected wave amplitude for different defects, the structure of the PFSH-EMAT is fixed, and only the size and shape of the defect are adjustable. Through numerical simulations, the reflected wave amplitudes of different defects are shown in Fig. 3(b) and (c). Fig. 3(b) demonstrates the results of cuboid defects with different sizes. The reflected wave amplitude increases with defect length l and width w . It could be explained that a larger l will increase the reflection cross section of the defect so that the total energy of the reflected wave is increased. It is well-known that the amplitude of the ultrasonic-guided wave decreases as the propagation distance increases. Specifically, increasing the width w of the defect is equivalent to shortening the transmit distance of the SH-guided waves, so the energy loss is reduced. For cylinder defects with different radii r shown in Fig. 3(c), the reflected wave amplitude increases antiparabolically with the defect radius. Since the center of the cylindrical defect is at the focal point, the main beam of the SH wave returns along the incident path, so the defect radius only affects the attenuation of the amplitude of the reflected SH-guided waves. Therefore, it could be seen that the

shape of the defect cannot be fully identified only by the amplitude of the axial reflection signal.

C. Characteristics of Receiving Circle

In order to accurately identify the shape of the defect, the concept of the receiving circle is introduced. The receiving circle is defined as a virtual circle with a focal point as the center and a radius of a certain length. The purpose is to obtain the maximum value of the defect reflection signal received at each point on the circle, thereby obtaining the reflection, scattering, and transmission signals of the SH-guided waves. Fig. 4 shows the circumferential scatter diagrams of the cuboid defects with different sizes and Fig. 5 shows the circumferential scatter diagrams of the cylinder defects with different radii through simulation. In these diagrams, the radial axis corresponds to the received ultrasonic signal amplitude. Besides, all signals on the acceptance circle for each time step are plotted and connected together until all time steps are plotted. Since the signal amplitude is proved to be challenging to judge the shape of a defect, each of the circumferential scattered patterns is normalized to their respective maximum values for comparison. In addition, the 90° direction of the receiving circle is defined as the direction of the SH-guided wave incident along the x-axis. Accordingly, 0° – 180° is the direction of the reflected wave, and 181° – 360° (0°) is the direction of the transmitted wave.

Fig. 4 shows that as the length l of the cuboid defect increases, the relative wave amplitude in the 270° direction decreases, that

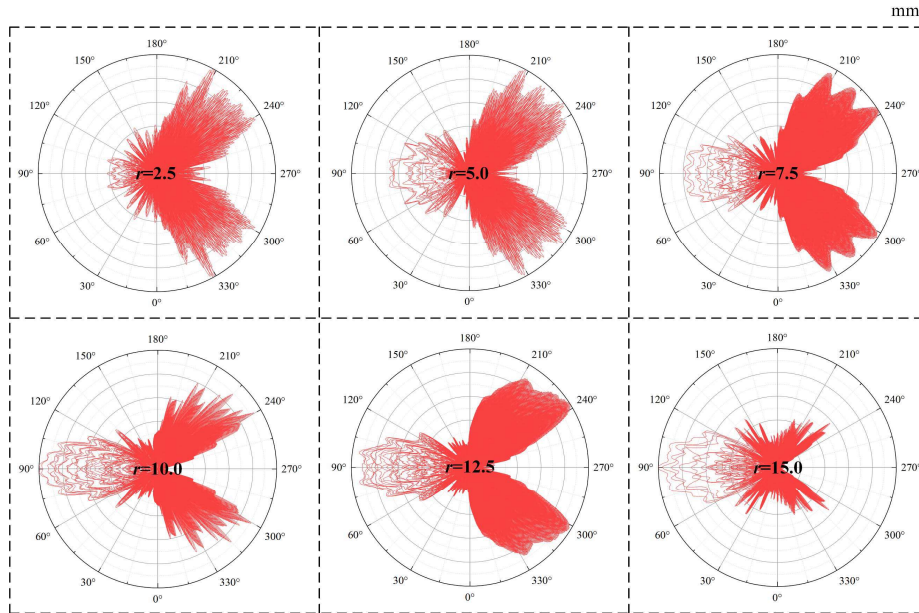


Fig.5. Circumferential scatter diagrams of the cuboid defects with different sizes..

is, the transmission ratio of the SH-guided wave decreases. Also, as the width w of the cuboid defect increases, the scattering angle of the reflected wave in the 90° direction is reduced, that is, the beam of the reflected wave becomes more concentrated. For cylinder defects, Fig. 5 shows that the reflected beam is substantially distributed in the range of 60° – 120° , which coincides with the preset 60° aperture angle of the coils. As the radius of the cylindrical defect increases, the proportion of transmitted waves in the 270° direction gradually decreases, and the proportion of reflected waves increases in the range of 60° – 120° . Moreover, the ratio of transmitted waves in the ranges of 200° – 240° and 300° – 340° also decreases substantially. By comparing Fig. 4 with Fig. 5, it could be found that the reflected wave of the cuboid defect has a range of 75° – 105° . The reflected beam of the cuboid defect is more concentrated than that of the cylindrical defect. Accordingly, this difference could effectively distinguish the shape of the defect.

IV. EXPERIMENTS

A. Experimental Validation

In the detection of the aluminum plate defects with the use of SH-guided waves, in order to enable a full description of plate defects, it is necessary to obtain the circumferential scattering results after the guided waves reach defects. Accordingly, in this study, a single PFSH-EMAT is used to excite the SH-guided wave, and 12 receiving probes are used to measure the scattered signals at various positions, as shown in Fig. 6. The upper probe is defined as No. 1, and the No. 2–12 probes are defined in a clockwise direction with an interval angle of 30° . The radius of the receiving circle is 30 mm, and the center is the focal point of the PFSH-EMAT. In the experiment, the focal length of the transducer is 100 mm. RPR-4000 is widely used as an ultrasonic excitation source and receiving device in ultrasonic-guided wave detection. It transmitted pulses of a specified waveform (burst signal) and passed them through the matching impedance

to the transmitter. The data of all the receiving probes were received by the RPR-4000 successively and displayed on the oscilloscope and the personal computer (PC).

For the cuboid defect with 10 mm length and 1 width, Fig. 7 shows the received signal of the No. 10 probe in the experiment, and its maximum value normalizes the signal. Moreover, simulation is also processed under the same conditions. It is shown that the simulation result shows good agreement with that in the experiment, in addition to the boundary reflected waves calculated from the simulation. Fig. 8 shows the circumferential scatter diagram of the normalized received signal from all the probes in the experiment as well as the results on the receiving circle in the simulation.

B. ML-Based Feature Extraction and Defect Quantification

Considering the abovementioned experimental results and the defect feature judgment method, the following feature extraction strategy can be established. Fig. 9 shows the relationship between the signal intensity measured by the 12 receiving probes and their positions in the experiment. Since the transmitting and receiving probes and defects are all symmetrical along the axis of 90° – 270° , only probes 1, 2, 3, 4, 10, 11, and 12 are considered. In the classification of defects, according to the characteristics of the obtained circumferential scatter diagrams, it can be found that the amplitude of the No. 2 probe (hereinafter referred to as “2”) has a greater correlation with the defect type. In addition, in the defect size quantification, for cuboid defects, its length is related to 4 and its width is related to 11; for cylinder defects, its radius is related to 10, and also related to 2 and 3. Therefore, the features A-D can be extracted as: A represents 10, B represents 11, C represents mean value of 2 and 3, and D, represents 4, as shown in Fig. 9. In general, the feature extraction of the experimental data for defect classification and quantification is achieved, and then these data features are fed to NN to verify the effectiveness of the proposed method.

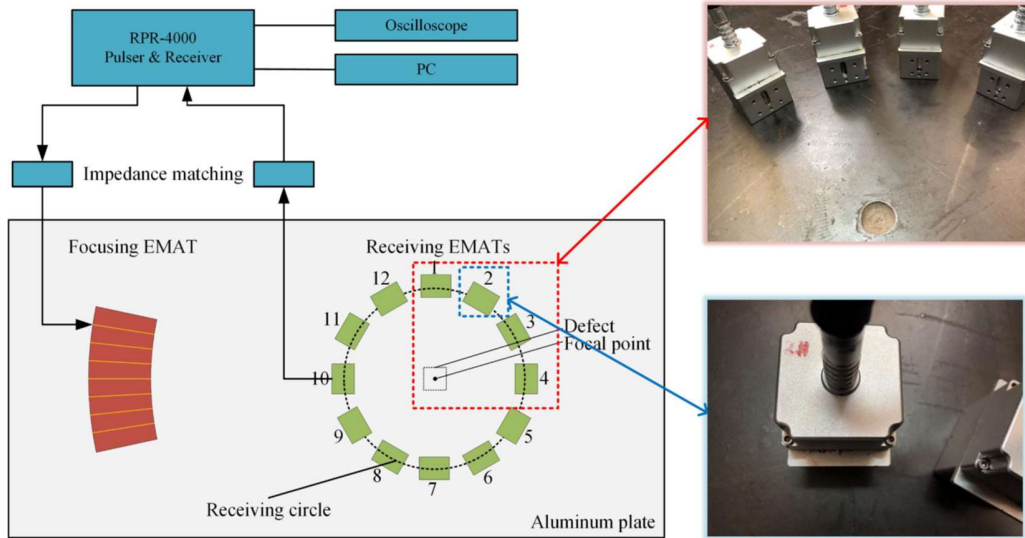


Fig. 6. Experiment configuration of the PFSH-EMAT to detect defects with different shape and sizes.

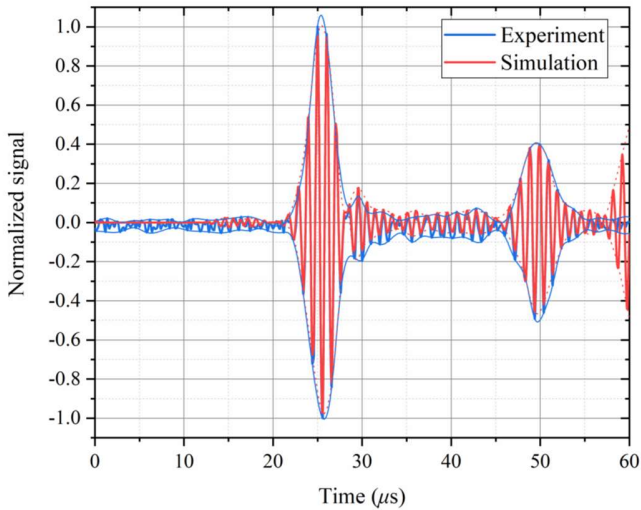


Fig. 7. Simulated and experimental results for the axial reflected wave of a cuboid defect with 10 mm length and width for #10 probe.

In the experiment, the length and width of the processed cuboid defects are 5, 7, 9, 11, 13, and 15 mm, and there are 36 in total; the radius of the processed cylinder defects is 2.5–15 mm with a step of 0.5 mm, and there are 26 in total, and all data are normalized. Besides, before feeding the feature values to NN, the normalization method is used in data preprocessing. To improve the generalization capability of the network, the data set is divided into training set, validation set, and test set at 50:10:6. To further increase the number of trainable data set, the k-fold cross-validation method is applied in this work. Therefore, the data set can be randomly divided into $k = 6$ packets, one of which is used as the validation set each time, and the remaining five packets are used as the training set for training. The software environment in network training is TensorFlow 2.2, Cuda 10.1, and Python 3.8; the hardware environment is i9-9900 (CPU), RTX2060 (GPU).

Fig. 10 shows the two NNs we constructed. The network shown in Fig. 10(a) uses a single hidden layer structure,

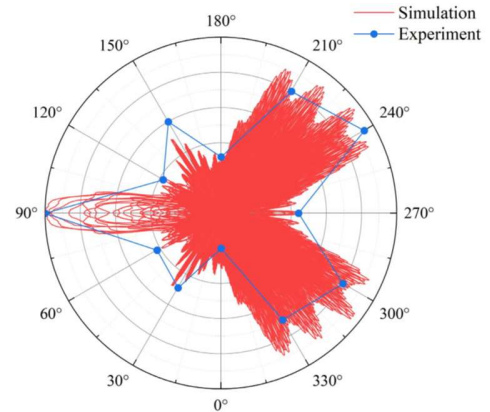


Fig. 8. Circumferential scatter diagram of the normalized received signal from all the probes in the experiment and simulation

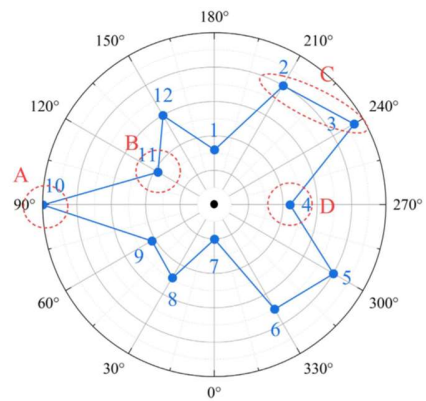


Fig. 9. Relationship between the normalized signal intensity measured by the 12 receiving probes and their positions, and the selection method of the four features is indicated by the red dotted circles and the red letters A, B, C, and D.

and the output is probalized through a SoftMax activation function to determine the type of defect. Besides, the learning rate of the network is set to 0.001, and the categorical

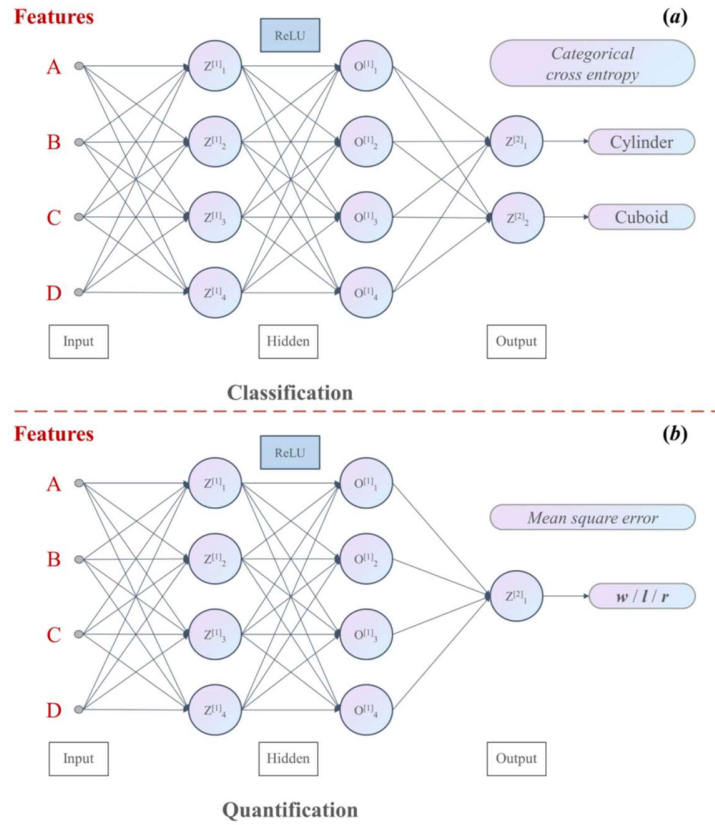


Fig. 10. Defect classification and quantification NN's structures.

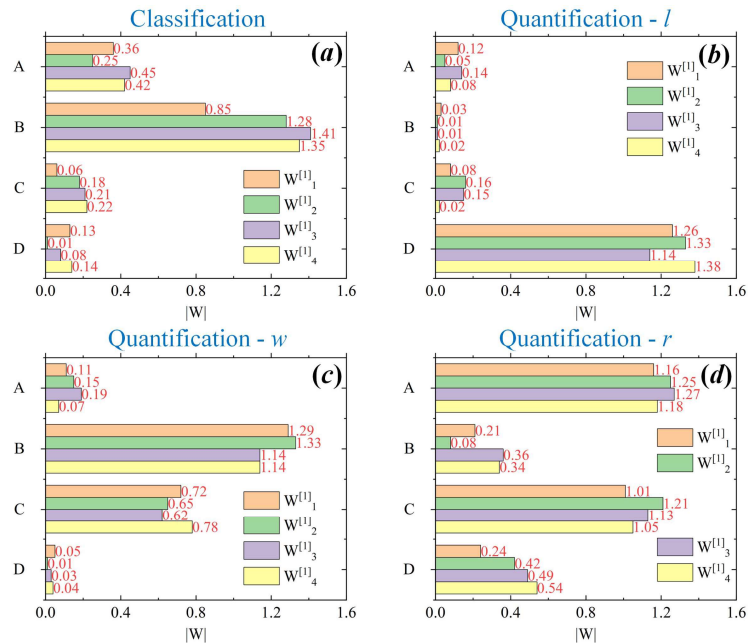


Fig. 11. Absolute values of the network weight parameters, respectively for the classification network and the three defect quantification networks. In the figure, different colors represent different neurons, such as $W^{[1]_1}, W^{[1]_2}, W^{[1]_3}, W^{[1]_4}$; the weights of neurons connected to each feature value are divided into the same group, such as A, B, C, D. (a) Classification network. Quantification networks for (b) length, (c) width, and (d) radius estimation.

cross-entropy loss function is used. Fig. 10(b) has a similar structure to Fig. 10(a), but the problem it solves is not a defect classification problem but a regression calculation of quantification of size. Therefore, the loss of the network is

selected as a mean square error, and the network is selected as a mean square error, and the network is trained according to different defect types (cylinder and cuboid) and size attributes (length, width, and radius). The test results show that the

training accuracy and test accuracy of the classification NN shown in Fig. 10(a) have reached 99.91%. The average training error of the quantized NN shown in Fig. 10(b) is 0.83%, and the average test error is 1.25%. The “error” here represents the error percentage between the quantized size and the actual size. Therefore, the feature extraction method proposed in this article can effectively achieve the accurate ML-based classification and quantification of defects.

Based on the above method, the correlation of defect features can be verified by extracting the weight parameters of the trained networks. Fig. 11 shows the absolute values of the network weight parameters, respectively for the classification network and the three defect quantification networks. It can be found from the figure that feature B is closely related to the defect type, followed by features A, C, and D. Besides, in the quantification of defect length for cuboid defects, feature D is obviously dominant; in the quantification of defect width for cuboid defects, feature B plays a major role, followed by C while A and D have limited contributions. For cylinder defect quantification, features A and C have close contributions, followed by D and B. From the corresponding relationship between the weight of the NN and the extracted features, it can be seen that the feature extraction method proposed in this article is effective and consistent with the simulation and experimental results. Furthermore, the defect classification and quantification problems of PFSH-EMAT based on the circumferential scatter diagrams can be solved by the proposed feature extraction and ML methods.

V. CONCLUSIONS

In this work, the defects detection of different shapes and sizes by PFSH-EMAT with the use of PPM is studied through FEM and experiment. The reflected waves of the cuboid and cylindrical through-hole defects are analyzed by the axial detection and the signal of the receiving circle. Reflected signal amplitudes from different defects are investigated. For cuboid defects with different sizes, the reflected wave amplitude increases with defect length l and width w . For cylinder defects with different radii r , the reflected wave amplitude increases antiparabolically with the defect radius. In order to further distinguish the shape of the defect, circumferential scatter diagrams are introduced and studied. As the length l of the cuboid defect increases, the relative wave amplitude in the 270° direction decreases. Besides, as the width w of the cuboid defect increases, the scattering angle of the reflected wave in the 90° direction is reduced. For cylinder defects, the reflected beam is substantially distributed in the range of 60° – 120° , which is the same as the coil’s aperture angle. As the radius of the cylindrical defect increases, the proportion of the transmitted wave in the 270° direction gradually decreases, and the proportion of the reflected wave increases in the range of 60° – 120° . Besides, the ratio of transmitted waves in the ranges of 200° – 240° and 300° – 340° is also significantly reduced. Therefore, these differences could effectively distinguish the shape of different defects.

In addition, to verify the above results, this article also describes the defect classification and quantification method by extracting the features of the experiment data, and using these features to train a NN. The results show that the proposed defect

classification method has an accuracy close to 100%, and an error of less than 1.5% in defect quantification. Besides, by analyzing the weights of the extracted neurons, it can be shown that the defect identification scheme based on the simulation results obtained in this work is reasonable.

REFERENCES

- [1] X. Jia and Q. Ouyang, “Optimal design of point-focusing shear vertical wave electromagnetic ultrasonic transducers based on orthogonal test method,” *IEEE Sensors J.*, vol. 18, no.19, pp. 8064-8073, Oct. 2018.
- [2] R. Ribichini, F. Cegla, P. B. Nagy, and P. Cawley, “Experimental and numerical evaluation of electromagnetic acoustic transducer performance in steel materials,” *NDT & E Int.*, vol. 45, no. 1, pp. 32-38, Jan. 2012.
- [3] C. B. Thring, Y. Fan, and R. S. Edwards, “Multi-coil focused EMAT for characterization of surface-breaking defects of arbitrary orientation,” *NDT & E Int.*, vol.88, pp. 1-7, Jun. 2017.
- [4] S. Wang, S. Huang, Y. Zhang, and W. Zhao, “Multiphysics modelling of a Lorentz force-based meander coil electromagnetic acoustic transducer via steady-state and transient analysis,” *IEEE Sensors J.*, vol. 16, no.17, pp.6641-6651, Sep.2016.
- [5] H. M. Seung, C. I. Park, and Y. Y. Kim, “An omnidirectional shear-horizontal guided wave EMAT for a metallic plate,” *Ultrasonics*, vol.69, pp.58-66, Jul. 2016.
- [6] S. Huang, L. Peng, Q. Wang, S. Wang, and W. Zhao, “An opening profile recognition method for magnetic flux leakage signals of defect,” *IEEE Trans. Instrum. Meas.*, vol. 68, no. 6, pp. 2229-2236, Jun. 2019.
- [7] C. Ye, Y. Wang, and Y. Tao, “High-density large-scale TMR sensor array for magnetic field imaging,” *IEEE Trans. Instrum. Meas.*, vol.68, no.7, pp.2594-2601, Jul. 2019.
- [8] D. Mirshekar-Syahkal and R. F. Mostafavi, “1-D probe array for ACFM inspection of large metal plates,” *IEEE Trans. Instrum. Meas.*, vol.51, no.2, pp.374-382, Apr. 2002.
- [9] H. Ogi, M. Hirao, and T. Ohtani, “Line-focusing of ultrasonic SV wave by electromagnetic acoustic transducer,” *J. Acoust. Soc. Amer.*, vol. 103, no.5, pp.2411-2415, May 1998.
- [10] N. Lunn, S. Dixon, and M. D. G. Potter, “High temperature EMAT design for scanning or fixed point operation on magnetite coated steel,” *NDT & E Int.*, vol.89, pp.74-80, Jul. 2017.
- [11] R. Ribichini, F. Cegla, P. Nagy, and P. Cawley, “Study and comparison of different EMAT configuration for SH wave inspection,” *IEEE Trans. Ultrason., Ferroelectr., Freq. Control*, vol. 58, no.12, pp. 2571-2581, Dec.2011.
- [12] X. Zhao and J. L. Rose, “Guided circumferential shear horizontal waves in an isotropic hollow cylinder,” *J. Acoust. Soc. Amer.*, vol.115, no.5, pp.1912-1916, May 2004.
- [13] C. F. Vasile and R. B. Thompson, “Excitation of horizontally polarized shear elastic waves by electromagnetic transducers with periodic permanent

- magnets,” *J. Appl. Phys.*, vol.50, no.4, pp.2583-2588, Apr. 1979.
- [14] M. Hirao and H. Ogi, “An SH-wave EMAT technique for gas pipeline inspection,” *NDT & E Int.*, vol.32, no.3, pp.127-132, Apr. 1999.
- [15] H. Sun, S. Wang, S. Huang, Q. Wang, and W. Zhao, “Point-focusing of shear-horizontal wave using fan-shaped periodic permanent magnet focusing coils EMAT for plate inspection,” *IEEE Sensors J.*, vol. 19, no.12, pp.4393-4404, Jun. 2019.
- [16] H. Sun, S. Huang, Q. Wang, S. Wang, and W. Zhao, “Improvement of unidirectional focusing periodic permanent magnet shear-horizontal wave electromagnetic acoustic transducer by oblique bias magnetic field,” *Sens. Actuators A, Phys.*, vol 290, pp.36-47, May 2019.
- [17] S. L. Huang, H. Y. Sun, Q. Wang, S. Wang, and W. Zhao, “Unidirectional focusing of horizontally polarized shear elastic waves electromagnetic acoustic transducers for plate inspection,” *J. Appl. Phys.*, vol. 125, no.16, Apr.2019, Art. no. 164504.
- [18] J.-H Lee and D.-H. Kim, “Integrity evaluation of pipe welding zones using wavelet transforms, and specific sensitivities based on SH-EMAT pulse-echo method,” *Int. J. Precis. Eng. Manuf.*, vol.15, no.10, pp.2051-2057, Oct. 2014.
- [19] P. A. Petcher and S. Dixon, “Weld defect detection using PPM EMAT generated shear horizontal ultrasound,” *NDT & E Int.*, vol.74, pp.58-65, Sep.2015.
- [20] R. Murayama, S. Makiyama, M. Kodama, and Y. Taniguchi, “Development of an ultrasonic inspection robot using an electromagnetic acoustic transducer for a Lamb wave and an SH-plate wave,” *Ultrasonics*, vol.42, nos.1-9, pp.825-829, Apr.2004.
- [21] X. Song and G. Qiu, “Optimization of a focusable and rotatable shear-wave periodic permanent magnet electromagnetic acoustic transducers for plate inspection,” *Sensors*, vol.17, no. 12, pp. 2722, Nov.2017.
- [22] Nurmalia, N. Nakamura, H. Ogi, M. Hirao, and K. Nakahata, “Mode conversion behavior of SH guided wave in a tapered plate,” *NDT & E Int.*, vol.45, no.1, pp. 156-161, Jan. 2012.
- [23] I. Guyon, *Feature Extraction: Foundations and Applications*, 1st ed. New York, NY, USA: Springer, 2006.
- [24] F. C. Cruz, E. F. S. Filho, M. C. S. Albuquerque, I. C. Silva, C. T. T. Farias, and L. L. Gouvêa, “Efficient feature selection for neural network based detection of flaws in steel welded joints using ultrasound testing,” *Ultrasonics*, vol. 73, pp.1-8, Jan. 2017.
- [25] L. Peng, H. Sun, S. Wang, Q. Wang, W. Zhao, and S. Huang, “Defect detection and identification of point-focusing shear-horizontal EMAT for plate inspection,” in *Proc. Conf. Precis. Electromagn. Meas. (CPEM)*, Aug. 2020, pp. 1-2.
- [26] H. Sun et al., “Point-focusing shear-horizontal guided wave EMAT optimization method using orthogonal test theory,” *IEEE Sensors J.*, vol. 20, no. 12, pp.6295-6304, Jun. 2020.
- [27] S. Huang et al., “Characteristics of T (0,1) guided-wave point-focusing electromagnetic acoustic transducer for pipe inspection,” *IEEE Sensors J.*, vol. 20, no.6, pp.2895-2903, Mar.2020.
- [28] T. Takishita, K. Ashida, N. Nakamura, H. Ogi, and M. Hirao, “Development of shear-vertical-wave point-focusing electromagnetic acoustic transducer,” *Jpn. J. Appl. Phys.*, vol. 54, no. 7S1, P. 07HC04, 2015.
- [29] N. Nakamura, K. Ashida, T. Takishita, H. Ogi, and M. Hirao, “Inspection of stress corrosion cracking in welded stainless steel pipe using point-focusing electromagnetic-acoustic transducer,” *NDT & E Int.*, vol.83, pp.88-93, Oct.2016.